

# Tunable Band Gaps in MUV-10(M): A Family of Photoredox-Active MOFs with Earth-Abundant Open Metal Sites

Kevin Fabrizio<sup>†</sup>, Konstantinos A. Lazarou<sup>†</sup>, Lillian I. Payne, Liam Twight,

Christopher H. Hendon\*, Carl K. Brozek\*

<sup>†</sup> equal contribution

*Department of Chemistry and Biochemistry, Material Science Institute,*

*University of Oregon, Eugene, OR 97403*

Email: chendon@uoregon.edu, [cbrozek@uoregon.edu](mailto:cbrozek@uoregon.edu)

---

**Abstract.** Titanium-based metal—organic frameworks (Ti-MOFs) attract intense research attention because they can store charges in the form of  $\text{Ti}^{3+}$  and they serve as photosensitizers for co-catalysts through heterogeneous photoredox reactions at the MOF-liquid interface. Both charge storage and charge transfer depend on redox potentials of the MOF and the molecular substrate, but the factors controlling these energetic aspects are not well understood. Additionally, photocatalysis involving Ti-MOFs relies on co-catalysts rather than the intrinsic Ti reactivity in part because Ti-MOFs with open metal sites are rare. Here, we report that the class of Ti-MOFs known as MUV-10 can be synthetically modified to include a range of redox-inactive ions with flexible coordination environments that control the energies of the photoactive orbitals. Lewis acidic cations installed in the MOF cluster ( $\text{Cd}^{2+}$ ,  $\text{Sr}^{2+}$ , and  $\text{Ba}^{2+}$ ) or introduced to the pores ( $\text{H}^+$ ,  $\text{Li}^+$ ,  $\text{Na}^+$ ,  $\text{K}^+$ ) tune the electronic structure and band gaps of the MOFs. Through use of optical redox indicators, we report the first direct measurement of the Fermi levels (redox potentials) of photoexcited MOFs in situ. Taken together, these results explain the ability of Ti-MOFs to store charges and provide design principles for achieving heterogeneous photoredox chemistry with electrostatic control.

---

## Introduction

The frontier orbital energies of photocatalysts and molecular substrates dictate key aspects of photoredox reactions, ranging from the thermodynamic driving forces of charge transfer to the wavelengths necessary for photoexcitation.<sup>1–4</sup> Although solid-state materials benefit from greater stability compared to homogeneous systems, defining the energetic positions of relevant orbitals,

such as the band-edge potentials, is often complicated by compositional defects that dominate the electronic structures.<sup>5,6</sup> Studying site-isolated metal centers in crystalline solids has therefore become an important strategy for investigating interfacial reactivity with molecular control. Whereas the active sites of conventional heterogeneous catalysts can be ill-defined, crystallographic metal centers in metal-organic frameworks (MOFs) combine the atomic precision of molecules with the convenience of solids. In place of typical organic linkers that bridge metal cluster “nodes” in MOFs, such as 1,4-benzenedicarboxylate, “metalloligands” offer an effective approach for installing precise catalytic species. Metalloligands are constructed by functionalizing well-studied homogeneous catalysts with carboxylates or other binding groups to repurpose them as MOF linkers.<sup>7–9</sup> Although they boast improved stabilities, metalloligands exhibit reactivity patterns that still resemble the chemistry of the homogeneous analogs. When viewed as discrete coordination complexes, the metal nodes of MOFs, on the other hand, often exist without molecular precedent,<sup>10</sup> thereby enabling unusual small molecule reactivity,<sup>11</sup> the stabilization of reactive intermediates,<sup>12</sup> and impressive catalytic performance.<sup>13,14</sup> For example, the family of M-MFU-4l (M = Ti, V, Cr, Ni, Zn) materials achieve ethylene oligomerization and polymerization activities superior to other homogeneous or heterogeneous catalysts.<sup>13,15–18</sup> MOF metal nodes therefore offer a unique platform for studying interfacial heterogeneous reactivity, whether for uncovering fundamental parameters difficult to pinpoint in less precise heterogeneous systems, e.g., TiO<sub>2</sub>, or to discover entirely new chemical transformations. Whereas most reports of catalysis at MOF metal nodes have focused on thermochemical and electrochemical reactions,<sup>19–21</sup> investigations into their photochemical reactivity typically involve co-catalysts. In these systems, photoexcited charges migrate from the MOF clusters to metalloligands, or to impregnated

nanoparticles and molecular catalysts, for subsequent reactivity.<sup>22–31</sup> By comparison, the intrinsic photoredox chemistry of MOF nodes remains underexplored.<sup>32–38</sup>

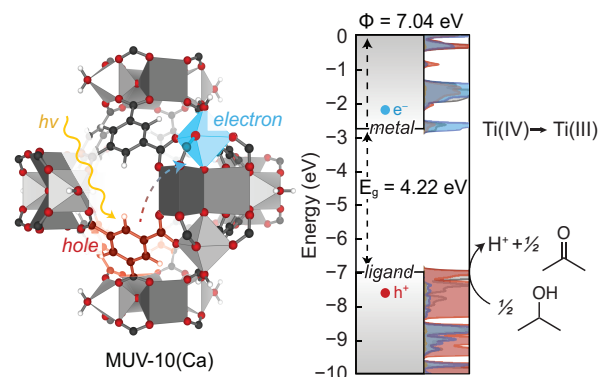


**Figure 1.** Molecular and band-diagram representation of the photodoping process in MUV-10(Ca).

Titanium-based MOFs (Ti-MOFs) offer a useful platform for studying heterogeneous photoredox chemistry. Because the low-lying empty d-orbitals of titanium dominate the conduction bands, the lowest-energy optical absorption features can be understood as linker-to-titanium charge transfer bands.<sup>39</sup> Synthetic manipulation of either metal or linker consequently leads to predictable changes to the band gap. For example, the amino-functionalized version of the material known as MIL-125-NH<sub>2</sub> (Ti<sub>8</sub>O<sub>8</sub>(OH)<sub>4</sub>(2-aminoterephthalate)<sub>6</sub>) displays a bandgap of 2.6 eV compared to the unfunctionalized variant, with a gap of 3.6 eV, resulting from the destabilization of the valence band, composed of linker-based orbitals upon amino functionalization.<sup>40,41</sup> Interestingly, many titanium MOFs are capable of storing charges upon photoexcitation in the presence of sacrificial reductants. For example, irradiating MUV-10(M) (Ti<sub>3</sub>M<sub>3</sub>(μ<sub>3</sub>-O)<sub>2</sub>(1,3,5-benzenetricarboxylate)<sub>4</sub>(H<sub>2</sub>O)<sub>6</sub>, M = Ca or Mn) with UV-visible light and excess ethanol leads to promotion of carboxylate-based electrons to empty titanium orbitals, with the resulting orbital holes quenched by oxidation of ethanol to furnish acetaldehyde and protons (**Fig. 1**). In the absence of air, such photochemical electronic doping (photodoping) leads to generation of indefinitely stable Ti<sup>3+</sup> centers that are charge-balanced by H<sup>+</sup>.<sup>39</sup> In other words, the

$\text{H}^+\text{-e}^-$  pairs become stabilized at the MOF clusters, rather than combine to form  $\text{H}_2$ . Similar attempts to photodope titanium MOFs featuring single Ti ions rather than multinuclear clusters does not lead to isolation of  $\text{Ti}^{3+}$ , however. To explain the unique ability of cluster-based Ti-MOFs to generate  $\text{Ti}^{3+}$  through photodoping, the Martí-Gastaldo group has proposed that clusters tend to produce photoexcited states where the electron localizes on the Ti atoms and the holes center on the linkers.<sup>42</sup> The spatial separation of excited-state charges therefore disfavors rapid electron-hole recombination, allowing ethanol to quench the linker-based hole and trap the  $\text{Ti}^{3+}$  state. The clusters in these materials typically contain inorganic oxos that bridge titanium centers. In support of the Martí-Gastaldo hypothesis, we propose that bridging oxos prevent  $\text{H}_2$  generation by serving as proton acceptors, thereby lowering the electrochemical potential of the  $\text{H}^+\text{-e}^-$  pair. In a similar vein, the Mayer group, has justified the charge storage capacity of titanium cluster MOFs in terms of cation-oxo electrostatic pairing stabilization.<sup>43,44</sup> Although MIL-125 nodes contain eight titanium centers, steady-state photoirradiation does not lead to quantitative reduction of all metal ions to  $\text{Ti}^{3+}$ , as evidenced by electron paramagnetic spectroscopy (EPR). Treatment of MIL-125 particles with sodium-based reductants, however, increases the average number of reduced metal ions per MIL-125 cluster, suggesting a strong cation-dependence and ion-pairing effect of charge storage in titanium MOFs.<sup>43</sup> The photoredox chemistry of MOFs, therefore, depends strongly on the chemical factors that control the electrochemical potentials of the resulting photoexcited charges. We therefore seek Ti-MOFs with OMSs and synthetic tunability for investigating the chemical factors that control photoredox activity.

In designing a system for studying heterogenous photoredox chemistry, the oxygen evolving complex (OEC) of Photosystem II (**Fig. 2**) provides a useful example because the  $\text{Mn}_4\text{O}_5\text{Ca}$  cluster accomplishes one of the most important examples of photoredox catalysis by

harnessing a carboxylate ligand field akin to typical MOF structures.<sup>45–48</sup> The OEC possesses several design principles for photoactive MOFs: In addition to being comprised of Earth-abundant metal ions, the redox-active  $\text{Mn}^{2+}$  bears an open metal site (OMS) and a redox-inactive  $\text{Ca}^{2+}$  ion influences the energetics of the OEC. Indeed, replacing  $\text{Ca}^{2+}$  with other alkaline Earth or transition metals leads to systematic shifts in the redox potentials of the native and biomimetic complexes, and in the redox chemistry of poloxometallates.<sup>49–52</sup> We hypothesize that Ti-MOFs containing redox-inactive metal ions would offer a convenient platform for photoredox chemistry with tunable electrochemical properties.

Here, we report that the Ti-MOF known as MUV-10(M)<sup>53</sup> can be expanded into an isostructural family of materials with clusters that incorporate a range of redox-inactive metal ions and Ti centers that support OMSs. Measurement of band gap (HOMO-LUMO) energies reveals that while the identity of the redox-inactive ions electrostatically shifts the Ti-based orbital energies, their dominant effect is to introduce structural flexibility that strongly impacts optical absorption profiles, especially in the presence of solvent. A similar effect is observed with the introduction of redox-inactive ions to the MOF pores, further illustrating their energetic influence on the orbital energies of photoredox materials. Importantly, the interpretation of these band gap energies required a reevaluation of the applicability of Tauc analysis, which will guide the future analysis of MOFs and other materials in general. Finally, the Fermi levels (electrochemical potentials) of photodoped MUV-10 were approximated using a contactless optical redox indicator

method, providing evidence of heterogeneous photoredox reactivity and a thermodynamic justification for the charge-storage properties of Ti-MOFs.

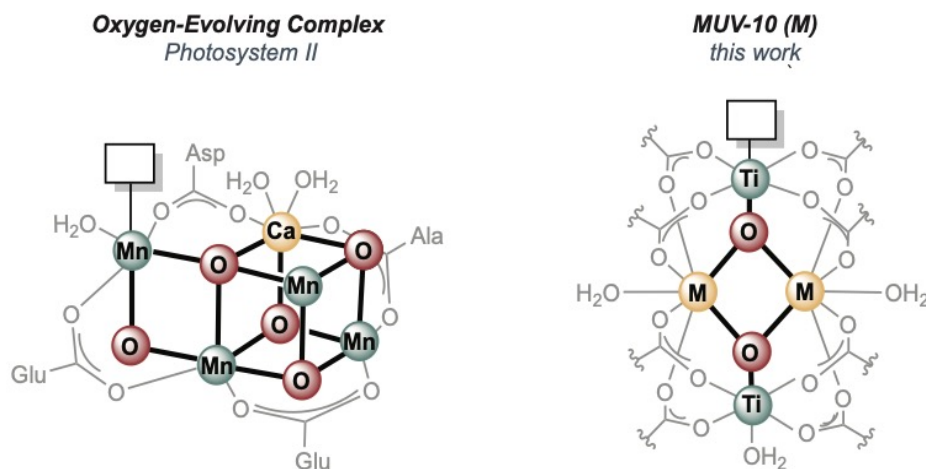


**Figure 2.** Comparison of the oxygen-evolving complex of Photosystem II and the heterometallic cluster of MUV-10(M). Redox-active metal sites noted in blue, bridging oxygens in red, redox-inactive metal sites in yellow, and open metal sites as boxes.

## Experimental

### *Materials and Equipment*

All manipulations were performed under an atmosphere of nitrogen in an LC Technology Glovebox or by using standard Schlenk techniques. All reagents were purchased from commercial sources and used without further purification. Solvents were purified using a LC Technologies SP-1 solvent purification system. PXRD patterns were recorded by dispersing activated dry samples on zero-background Si plates using a Bruker D2 Phaser, in the range of 3 to 35°  $2\theta$  using a copper K- $\alpha$  radiation source. N<sub>2</sub> gas sorption isotherms were collected on a Micromeritics ASAP 2020 Plus. X-ray fluorescence data was collected using a Rigaku ZSX Primus II wavelength dispersive X-ray fluorescence spectrometer with a rhodium X-ray source. IR spectra were collected on a Bruker Alpha II with an ATR attachment in a nitrogen filled glovebox and a Nicolet 6700 FT-IR spectrometer with an ATR attachment in open air. UV-vis measurements were performed using a PerkinElmer Lambda 1050 spectrophotometer with a Peltier-cooled InGaAs and PbS detector.

MUV-10(M) samples were diluted with BaSO<sub>4</sub> as a reference, loaded into a Harrick high temperature environmental chamber and attached to a Harrick praying mantis accessory to perform DRUV-vis measurements. The chamber was allowed to equilibrate at a set temperature from 25 °C to 350 °C for 30 minutes under dynamic vacuum before each measurement was taken at static vacuum.

#### *Preparation of MUV-10(Ca, Mn)*

MUV-10 (Ca) and MUV-10 (Mn) were synthesized according to a literature method.<sup>53</sup> ( Briefly, a solvothermal reaction of calcium chloride dihydrate (0.0176 g, 0.12 mmol) or manganese (II) chloride tetrahydrate (0.0238 g, 0.12 mmol), titanium (IV) isopropoxide (36 µL, 0.12 mmol) and trimesic acid (0.125 g, 0.595 mmol) in DMF (12 mL), using glacial acetic acid (3.5 mL) as a modulator for crystal growth, is conducted at 120 °C for 48 hours in a 50-mL Pyrex Schott bottle.

#### *Preparation of MUV-10(Ba, Sr, Cd)*

Following a procedure adapted from Castells-Gil et. al.,<sup>53</sup> trimesic acid (0.125 g, 0.60 mmol) and either barium chloride dihydrate (0.044 g, 0.18 mmol), strontium chloride hexahydrate (0.048 g, 0.18 mmol), or cadmium chloride hemi(pentahydrate) (0.041 g, 0.18 mmol) were added to a 50-mL Schott bottle dissolved in dry DMF (12 mL). The solution was then transferred to a benchtop N<sub>2</sub> glovebox, where glacial acetic acid (3.5 mL for Cd/Sr, and 5.0 mL for Ba) and titanium (IV) isopropoxide (36 µL, 0.12 mmol) were added, and the bottle was resealed. Then, the solution was heated in a fixed-temperature oven at 120 °C for 48 hours. The resulting white powder was centrifuged and washed three times sequentially with 20 mL clean DMF and methanol, and then dried under dynamic vacuum overnight at room temperature.

### *Fermi Level Estimation by Optical Redox Indicator*

In an N<sub>2</sub> glovebox, FeCp\*<sub>2</sub> was weighed into a Schlenk flask and dissolved in ca 5 mL hexanes. In air, benzoquinone was dissolved in ca 5 mL of ethyl ether, and HBF<sub>4</sub> was added. The FeCp\*<sub>2</sub> and benzoquinone solutions were combined by cannula transfer, creating a cloudy dark-green mixture. This solution was left to stir for one hour, and let stand for 30 minutes, yielding a green precipitate. The flask was transferred to a benchtop N<sub>2</sub> glovebox, where it was vacuum filtered and washed with dry hexanes (~40 mL). Once transferred into a standard N<sub>2</sub> glovebox, the powder was dissolved in dry MeCN. The concentration of the solution was tested via UV vis by way of a dilution of 300  $\mu$ L in 3 mL MeCN in an air-free quartz cuvette with pathlength 1 cm, and the concentration was determined to be 4.06 mM by the 30 minute irradiation absorbance value at 778 nm for an absorptivity coefficient of 488 L mol<sup>-1</sup> cm<sup>-1</sup>, according to prior studies of the [FeCp\*<sub>2</sub>]/ [FeCp\*<sub>2</sub>]<sup>+</sup> redox couple.<sup>54</sup> Similar to the previous experiment, 3 mg of MUV-10 (Ca) were added to 3 mL of stock [FeCp\*<sub>2</sub>]<sup>+</sup> in MeCN and 300  $\mu$ L of dry ethanol. The cuvette was irradiated with a mercury arc lamp, and the UV-vis spectra were recorded after allowing the powder to settle. After 1290 min of irradiation (21.5 hr) the vibrant green solution had turned yellow, indicating the complex's conversion to FeCp\*<sub>2</sub>.

### *Soaking MUV-10(Ca) in Nitrate Salts*

The impact of H<sup>+</sup> on MUV-10(M) was tested by soaking 1 mg of MUV-10(Ca) in 2 mL of 10<sup>-3</sup> M HNO<sub>3</sub> overnight (>16 h) and then measuring the diffuse reflectance spectrum. Similarly, the impact of different cations was examined by preparing suspensions consisted of 2 mL aqueous solutions of LiNO<sub>3</sub>, NaNO<sub>3</sub>, and KNO<sub>3</sub>, respectively together with 1 mg of MUV-10(Ca) such that the ratio of cation to Ti in the MOF would be 5:1. After every soaking experiment, a powder diffraction pattern was collected to ensure that the crystal lattice remained intact (**Fig. S23**).



## Results and Analysis

### *Preparation of the MUV-10(M) Isostructural Series.*

The Ti-MOF known as MUV-10(M), where M = Ca or Mn, was selected as a molecularly defined platform for studying heterogeneous photoredox chemistry. The heterobimetallic clusters of MUV-10(M) consist of two octahedral Ti(IV) centers bridged to two heterometals by inorganic oxos and trimesate carboxylate linkers (**Fig. 2**). By combining the carboxylate and aqueous ligand environments, metal-oxo architecture, redox-inactive heterometals, and photoactive Ti ions with OMSs therefore renders MUV-10(M) an ideal candidate for pursuing the design principles of the oxygen-evolving complex (OEC) of PSII. Just as the redox-inactive heterometal tunes the redox chemistry of OEC and molecular inorganic clusters, we sought to prepare analogs of MUV-10(M) with a range of metal ions, based on the hypothesis that they would influence the  $\text{Ti}^{4+/3+}$  reduction potential through electrostatic interactions. By building a library of MUV-10(M) variants, we planned to investigate the energetic effect of cations on the electronic structure of photoredox materials.

Three new MUV-10(M) derivatives (M = Ba, Sr, Cd) were prepared by a modified solvothermal synthesis. **Figure 3a** plots the powder X-ray diffraction (PXRD) patterns, confirming retention of the original MUV-10(Ca) structures. Attempts to synthesize MUV-10 solely from  $\text{Sr}^{2+}$ ,  $\text{Ba}^{2+}$ , or  $\text{Cd}^{2+}$  precursors yielded amorphous materials. We note that an attempt at post-synthetic cation exchange in MUV-10(M) was recently reported not to yield isostructural products.<sup>55</sup> Although relative peak intensities differ from the calculate patterns, similar discrepancies between experimental and theoretical Bragg intensities have been observed for MOF-5 prior to complete activation.<sup>56</sup> While attempts to incorporate  $\text{Mg}^{2+}$  to complete the series of alkaline Earth metals did not yield a crystalline product, a recent study demonstrated that the

inclusion of  $\text{Mg}^{2+}$  results in a separate MOF isostructural to the MIL-100 family.<sup>57</sup> We suspect that ionic radius is a critical determinant of isostructural MOF syntheses, given that the ionic radius for  $\text{Mg}^{2+}$  in a six-coordinate geometry is 0.72 compared to  $\text{Ca}^{2+} = 1.0$ ,  $\text{Mn}^{2+} = 0.83$ ,  $\text{Ba}^{2+} = 1.35$ ,  $\text{Sr}^{2+} = 1.18$ , and  $\text{Cd}^{2+} = 0.95$ .<sup>58</sup> Interestingly, computational methods in the seminal report on MUV-10(Ca, Mn) predicted that an MUV-10(Cd) variant would be the least thermodynamically favorable, and yet we demonstrate it can be prepared following similar procedures.  $\text{Cd}^{2+}$  was targeted in order to compare the energetic impact of a  $d^{10}$  transition metal ion in comparison to  $\text{Mn}^{2+}$ , which is  $d^5$ , and to expand upon examples of redox-inactive variants beyond alkaline Earth metals. X-ray fluorescence spectra of all powders confirmed that both metal ions incorporate into the structures (**Figure S1-S7**).

For further evidence of isostructural MUV-10(M) derivatives,  $\text{N}_2$  gas sorption isotherms were measured at 77 K for MUV 10(Ba, Sr, Cd) following activation under vacuum at 130 °C. **Figure 3b** plots both adsorption and desorption data, revealing the expected Type I isotherms and reversibility for all materials. Multi-point Brunauer-Emmett-Teller (BET) analysis yields specific

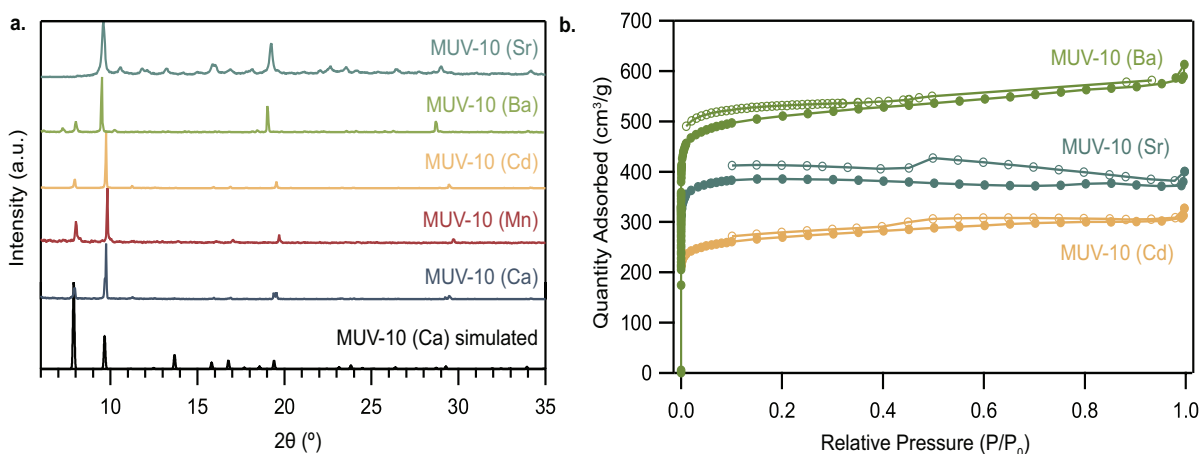


**Figure 3:** **a)** Powder X-ray diffraction patterns of MUV-10(M),  $\text{M} = \text{Ca}^{2+}$ ,  $\text{Mn}^{2+}$ ,  $\text{Cd}^{2+}$ ,  $\text{Ba}^{2+}$ , or  $\text{Sr}^{2+}$ . **b)**  $\text{N}_2$  gas sorption measurements of MUV-10(Sr, Ba, Cd) derivatives collected at 77 K. Adsorption curves are denoted by full circles and desorption by open circles.

surface areas of 1902.99, 1227.63, and 871.44 m<sup>2</sup>/g (2.89x10<sup>6</sup>, 1.68x10<sup>6</sup>, 1.27x10<sup>6</sup> m<sup>2</sup>/mol), for Ba, Sr, and Cd respectively. While the MUV-10(Cd) surface area is comparable to the original values of MUV-10(Ca, Mn) at 1041 and 940 m<sup>2</sup>/g, respectively, the Ba<sup>2+</sup> and Sr<sup>2+</sup> variants showed surprisingly high uptake. We hypothesize that their increased surface areas can be attributed to large ionic radii (1.35 and 1.18 Å, respectively), which may expand pores sizes, but also create linker vacancies through lattice strain.

#### *Generation of Photoactive Open Metal Sites.*

For insight into the structural stability of the new MUV-10(M) derivatives and for initial evidence that they support OMSs via removal of water ligands, we performed thermogravimetric analysis (TGA). All three derivatives (Ba, Sr, Cd) show thermal stability to 475 °C and significant weight loss below 150 °C: 21.03% for MUV-10 (Ba), 24.48% for MUV-10 (Sr), and 13.42% for MUV-10 (Cd) (**Fig. 4**). Based on the assumption that one water molecule coordinates to each metal in a formula unit of MUV-10(M), we would anticipate a weight loss of 6.65% for MUV-10 (Ba), 7.60% for MUV-10 (Sr), and 6.97% for MUV-10 (Cd) for complete removal of terminally bound aqua ligands. Because the actual weight losses for all three derivatives is markedly higher than

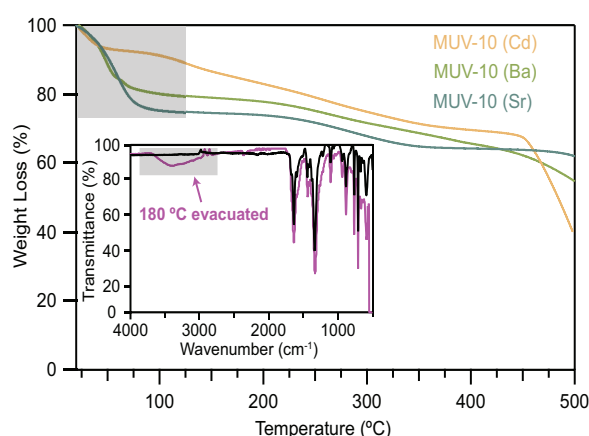


**Figure 4:** Thermogravimetric analysis for new MUV-10 (M) derivatives (Cd, Ba, Sr) showing a significant weight loss between 0-100 °C after solvent exchange and activation at elevated temperatures. Inset: IR spectra of as prepared MUV-10 (Ca) and activated MUV-10 (Ca) suggesting a loss of the -OH stretch in water at 3700-3000 cm<sup>-1</sup>.

expected, we attribute these weight changes to loss of pendant water molecules, interactions of the alkali earth metals with excess water (as evidenced by the difference in experimental weight losses between MUV-10(Ba, Sr)) and MUV-10(Cd)), and residual water/methanol mixtures from the pores. For direct evidence of OMS generation, we compared Fourier transform infrared (FT-IR) spectra of all derivatives before and after treatment with vacuum at 130 °C. **Figure 4** compares IR spectra of the as-prepared and evacuated materials, showing the disappearance of the broad peak associated with the –OH stretch of water. Given prior evidence from CO adsorption studies that water can be removed from the Ti sites of MUV-10(Ca),<sup>59</sup> these data suggest MUV-10(M) comprises an unusual family of photoactive MOF with OMSs.

*Electrostatic control of band gap energies.*

UV-vis spectra were collected *in situ* of all materials during evacuation and heating to probe changes of the titanium ligand field upon water removal and for evidence that varying the heterometal identities electrostatically tunes titanium redox potentials. Because the Ti 3d orbitals dominate the composition of Ti-MOF conduction bands, we reasoned that changes to the band gap energies can be interpreted in terms of alterations to the  $\text{Ti}^{4+/3+}$  redox potential. For example, if a chemical modification causes the conduction band edge to lower in energy and narrow the band gap, then the  $\text{Ti}^{4+/3+}$  redox potential therefore stabilized. **Figures 5a-e** plot UV-vis spectra of MUV-10(Ca, Mn, Cd, Sr, Ba) collected in diffuse-reflectance spectroscopy. The spectra compare the samples analyzed under ambient-pressure  $\text{N}_2$  at 25 °C *vs* dynamic vacuum while heating between 25 °C and 350 °C. By collecting spectra *in situ*, we were therefore able to monitor the dehydration and creation of OMSs in the MUV-10 family. Plotted in Kubelka-Munk units, all 25 °C spectra exhibit a gradual increase in absorption beginning around 3.0 eV and maximizing near 4.5 eV. When heated under dynamic vacuum to 350 °C, however, all samples show a significant

increase in absorption at lower energies, beginning around 2.0 eV. By assigning the peak

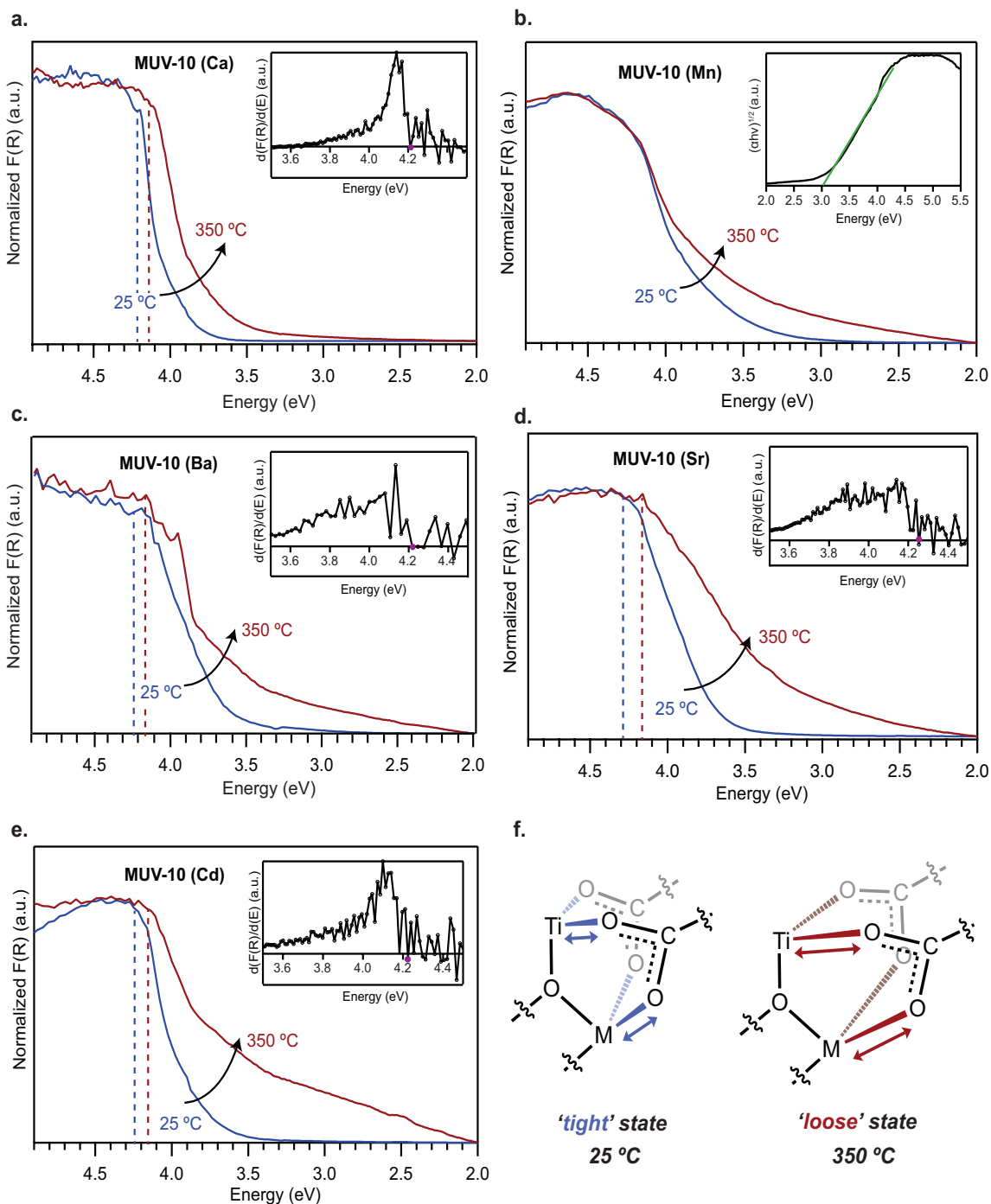


**Figure 5: a-e)** Variable temperature diffuse reflectance UV-vis-NIR spectra for MUV-10(Ca, Mn, Cd, Ba, Sr) to monitor dehydration. Dashed lines indicate band gap energies determined by derivative analysis (Ca, Ba, Sr, Cd) or Tauc plot analysis (Mn). Insets show derivative or Tauc plots. **f)** Scheme of 'tight' and 'loose' states of dynamic metal-carboxylate bonding in MUV-10 (M) cluster at high temperatures.

maximum to an O(2p)—Ti(3d) ligand-to-metal charge transfer (LMCT) band, dehydration and

varying the heterometal identities were expected to shift the  $\text{Ti}^{4+/3+}$  redox couples and, hence, peak maxima. The pronounced absorption tails at higher temperatures, however, were unexpected. Rather than simple shifts to band gap energies, we suspected that the low-energy absorption features arise from thermally activated distortions to the Ti ligand sphere, thereby creating transitions between midgap defect orbitals. With this in mind, the defects could be irreversibly formed, such as by water removal, or they could form reversibly, such as by thermally induced dynamic bonding between “tight” and “loose” configurations (**Fig. 5f**), as reported recently.<sup>60</sup> **Figure 6** shows that the absorption tailing across 20 °C to 250 °C is reversible, suggesting a thermodynamically controlled equilibrium process rather than an irreversible creation of defects. Consequently, assigning band gap energies and interpreting the electronic structures of MUV-10(M) materials depends on identifying the origin of such low-energy features.

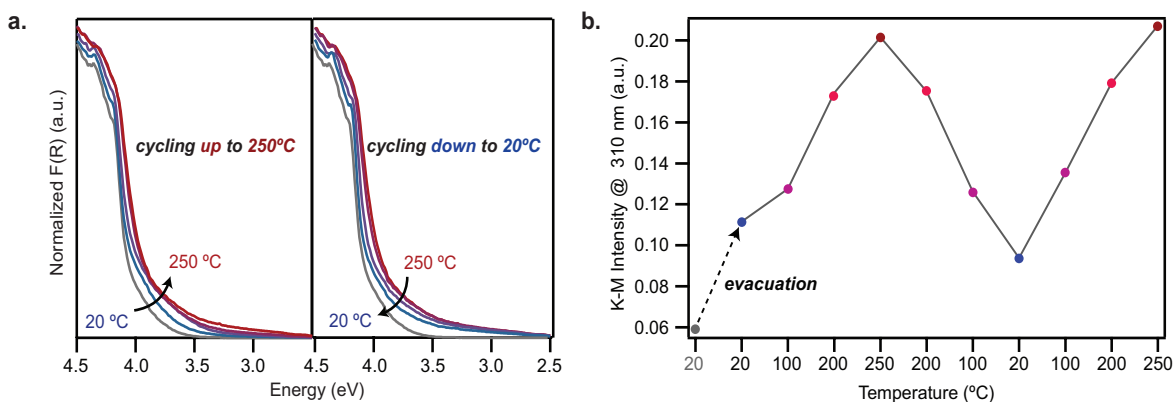


**Figure 6. a)** Diffuse reflectance UV-vis data of MUV-10(Ca) collected under dynamic vacuum and cycled between 20 – 250 °C. **b)** Kubelka-Munk intensities at 4.0 eV versus temperature.

Choosing methods for assigning band gap energies depends on whether low-energy absorption tails arise from the band edges or from mid-gap orbitals. On one hand, the peak maxima can be taken as the excitation of a valence-band electron to the conduction band. If many overlapping bands contribute to the absorption onset, however, the band gap energy can be determined from the intersection of the energy axis and a linear fit of the absorption edge, known

as Tauc Plot analysis. Superficially, the absorption profiles of all derivatives, except MUV-10 (Mn), display increased absorption at lower excitation energies, suggesting dehydration causes a considerable band gap narrowing of nearly 1.0 eV by Tauc analysis in the case of MUV-10(Cd). Increased absorption involves pronounced tailing of the optical bands rather than significant shifts to the band maxima, however. Understanding the origin of such drastic changes to optical absorption requires precise knowledge of the electronic structures of MUV-10(M) materials.

**Figure 7** shows the computed DOS diagrams for MUV-10(Ca) in different states of hydration. The “fully hydrated” structure was constructed with one H<sub>2</sub>O bound to each Ti and Ca metal site. The “partially hydrated” structures feature just a single H<sub>2</sub>O bound to each titanium atom and “dehydrated” includes no H<sub>2</sub>O ligands. Upon dehydration, the calculated band gaps narrow by ~100 meV from 4.22 to 4.11 eV. Inspection of the electronic structures suggests that the frontier orbitals remain largely intact and simply shift towards lower-energy potentials as a result of water removal. To compare these computed band gaps to experimental values, we attempted Tauc analysis of MUV-10(Ca) at 25 °C, which involved fitting the absorption band tails, yielding a gap of 3.83 eV. The difference between this value and the computed gap of 4.22 eV was outside the typical margin of error for this level of theory, however. Derivative analysis, on the other hand, produced a band gap of 4.21 eV, which is nearly identical to the computed value. The prominence of absorption tails at higher temperatures therefore cannot be attributed to a well-ordered structural change. We reasoned that the dynamic metal-linker bonding of MUV-10(Ca), as detailed previously,<sup>60</sup> could give rise to the absorption tail by creating mid-gap orbitals that arise from disorder around the MOF node. A thermally induced shift of the bonding equilibrium from “tight” to “loose” binding is also consistent with the reversibility evidenced in **Figure 6**.



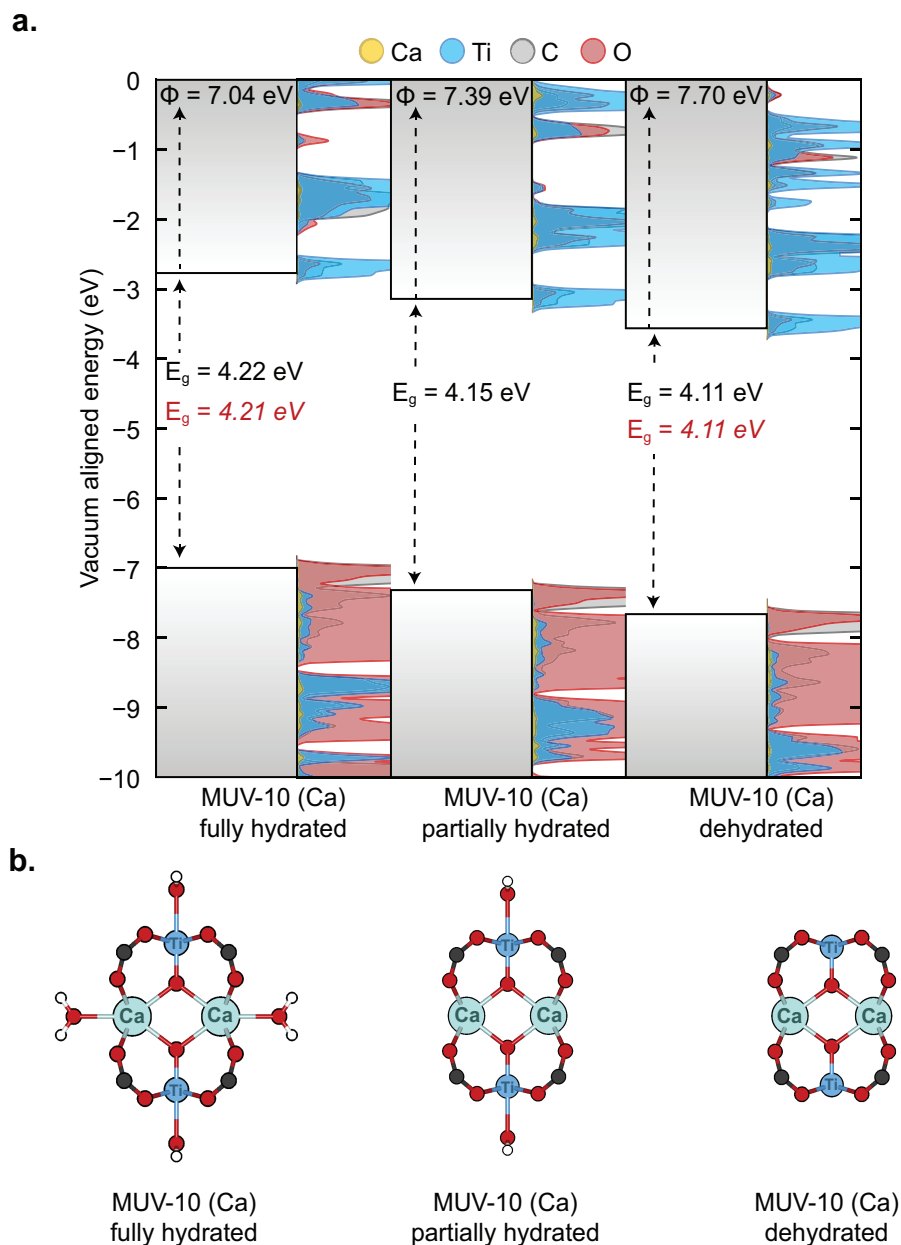


**Figure 7: a)** Density functional theory (DFT) density of states (DOS) calculations for “fully hydrated”\_MUV-10 (Ca), “partially hydrated” MUV-10 (Ca), and “dehydrated” MUV-10 (Ca). Experimental and computed band gap energies are shown in red and black, respectively. **b)** Geometry-optimized structures for three forms of MUV-10 (Ca) hydration.

To understand the effect of varying heterometals on the electronic structures of MUV-10(M) materials, we computed DOS diagrams of all “fully hydrated” MUV-10(M) derivatives (**Fig. 8**). Comparison of the MUV-10(Ca, Sr, Ba) electronic structures shows a clear electrostatic

influence of the alkaline Earth metals, with heavier elements exerting greater stabilization on frontier orbital energies. For example, replacing  $\text{Ca}^{2+}$  with  $\text{Ba}^{2+}$  causes the O-based valence band to shift by 50 meV and the Ti-based conduction band to stabilize by 140 meV. By Tauc analysis, comparison of computed band gap energies did not match experimental results, except for MUV-10 (Mn). Derivative analysis, however, yielded experimental band gap energies in close agreement with theory **Table 1**. These results suggest that the chemical factors contributing to the absorption tail do not arise from simple alterations to the heterometal identities. Instead, the optical band gaps of the MUV-10(Ca, Ba, Sr, and Cd) materials are best described as a valence-to-conduction band edge transitions, regardless of hydration state and presence of mid-gap orbitals. For example, in the case of MUV-10(Ca) the band gap energy determined by Tauc analysis is 0.40 eV less than expected, whereas derivative analysis is off within a margin of error (0.01 eV) for this technique. We propose that whereas most MUV-10 materials exhibit wide band-gap transitions appropriate for derivative analysis, band gap assignment of MUV-10(Mn) requires Tauc analysis because the multitude of ligand-field transitions overlap with the O(2p)—Ti(3d) absorption band.

**Table 1:** Comparison of experimentally determined band gap energies for fully hydrated MUV-10 (M) using Tauc analysis and derivative analysis, versus DFT calculated band gap energies.

MOF Name	$E_g$ Tauc (eV)	$E_g$ Deriv. (eV)	$E_g$ DFT (eV)
MUV-10 (Ca)	3.83	4.21	4.22
MUV-10 (Mn)	3.03	4.34	2.78
MUV-10 (Sr)	3.36	4.25	4.17
MUV-10 (Ba)	3.29	4.21	4.13
MUV-10 (Cd)	3.32	4.18	4.13

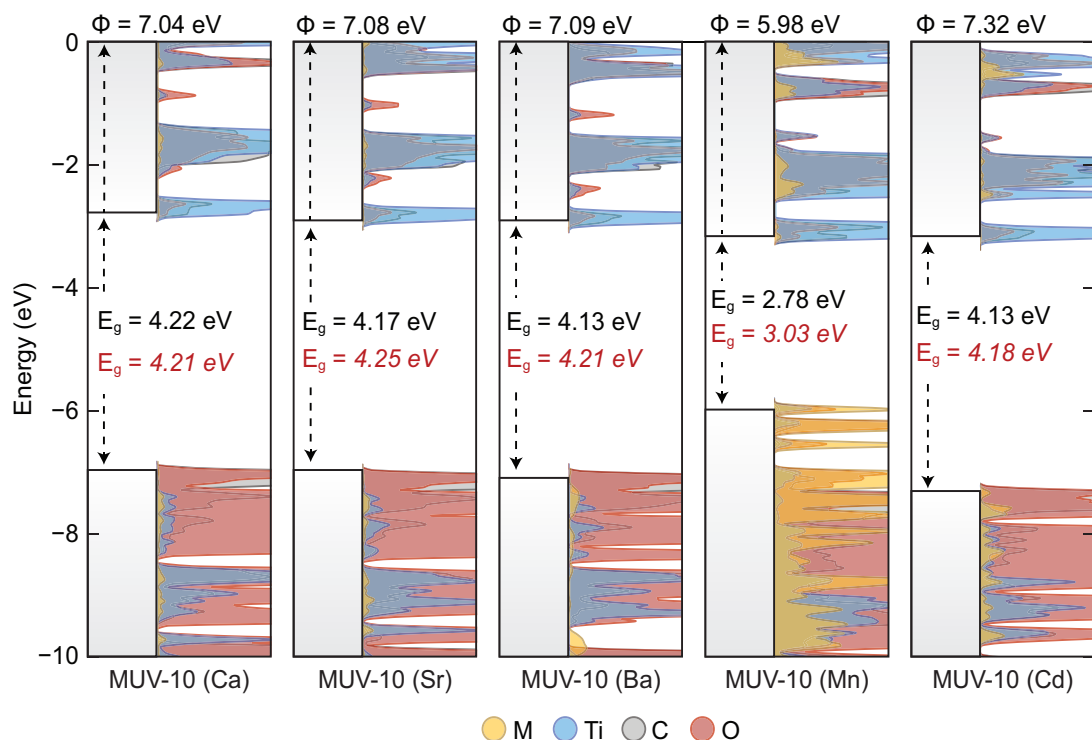


**Figure 8.** Density functional theory DOS calculations for all hydrated derivatives. Experimentally determined values shown in red, either by derivative analysis (Ca, Sr, Ba, Cd) or Tauc analysis (Mn).

Because proton-coupled electron transfer and, more broadly, ion-coupled charge transfer of Ti-MOFs has been described in terms of electrostatic interactions between soluble cations and MOF nodes, we investigated the impact of introducing cations to the MUV-10 (Ca) pores. In particular, we were interested in whether the electrostatic influence of cations could explain the high charge capacitance of Ti-MOFs, with recent evidence for  $\text{H}^+$  and  $\text{Na}^+$  coordination to the oxo-bridges of the  $\text{Ti}_8\text{O}_8$  molecular cluster analog of MIL-125.<sup>43</sup> Given the electrostatic impact of redox-inactive cations *within* the MUV-10 node, introducing soluble cations *outside* the node offers a means to compare the effect of cation location. After activation at 130 °C under dynamic vacuum, MUV-10 (Ca) was soaked in 0.1-M inorganic nitrate salt solutions ( $\text{LiNO}_3$ ,  $\text{KNO}_3$ ,  $\text{NaNO}_3$ ) and  $10^{-3}$ -M  $\text{HNO}_3$ . Stability and phase purity after cation treatment were confirmed by PXRD (Fig. S23). Following cation treatment, the optical absorption of all materials were analyzed

at 25 °C via diffuse reflectance UV-vis spectroscopy (**Fig. 9**). Rather than simple shifts to the band maxima, all spectra show the emergence of new, lower-energy absorption with the introduction of soluble cations. We hypothesized that the cations bind to the MOF nodes, causing a lowering in symmetry and, hence, the introduction of mid-gap orbitals that cause low-energy absorption. Although inappropriate for the wide-gap MUV-10(Ca) without cations, Tauc analysis is suitable for analyzing materials with overlapping bands arising from mid-gap orbitals. Compared to hydrated MUV-10(Ca) (3.83 eV), Tauc analysis of all cation-soaked samples indicates considerable narrowing of band gap energies, with  $\text{H}^+$ -MUV-10(Ca) showing a gap of just 3.22 eV. To explore the origin of this cation-induced effect, we computed the DOS for  $\text{H}^+$ -MUV-10(Ca) modeled by placing  $\text{H}^+$  near the nodes and allowing the structure to relax (**Fig. 10**). Compared with the DOS of hydrated MUV-10(Ca), the DOS of  $\text{H}^+$ -MUV-10(Ca) show the valence band destabilizing by 900 meV but the conduction band stabilizing 740 meV. Additionally, protonation breaks the energetic degeneracy of MUV-10(Ca) orbitals, causing the initially sparse electronic structure to spread into many inequivalent orbitals, indicating a lowering of symmetry. Indeed, the

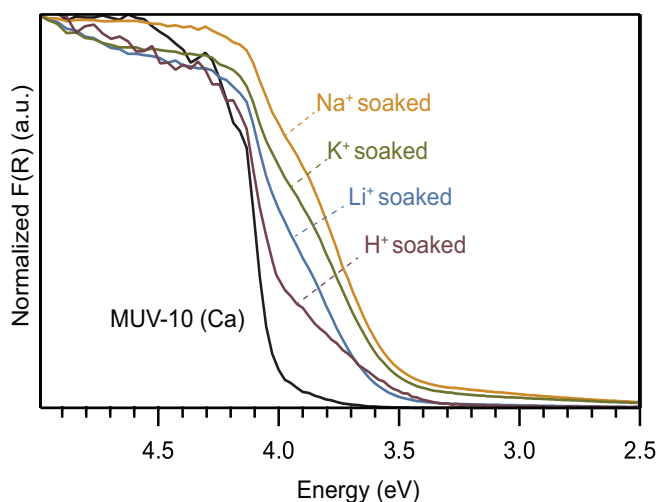


**Figure 9.** Diffuse reflectance UV-vis-NIR spectra of MUV-10(Ca) soaked with different nitrate salts.

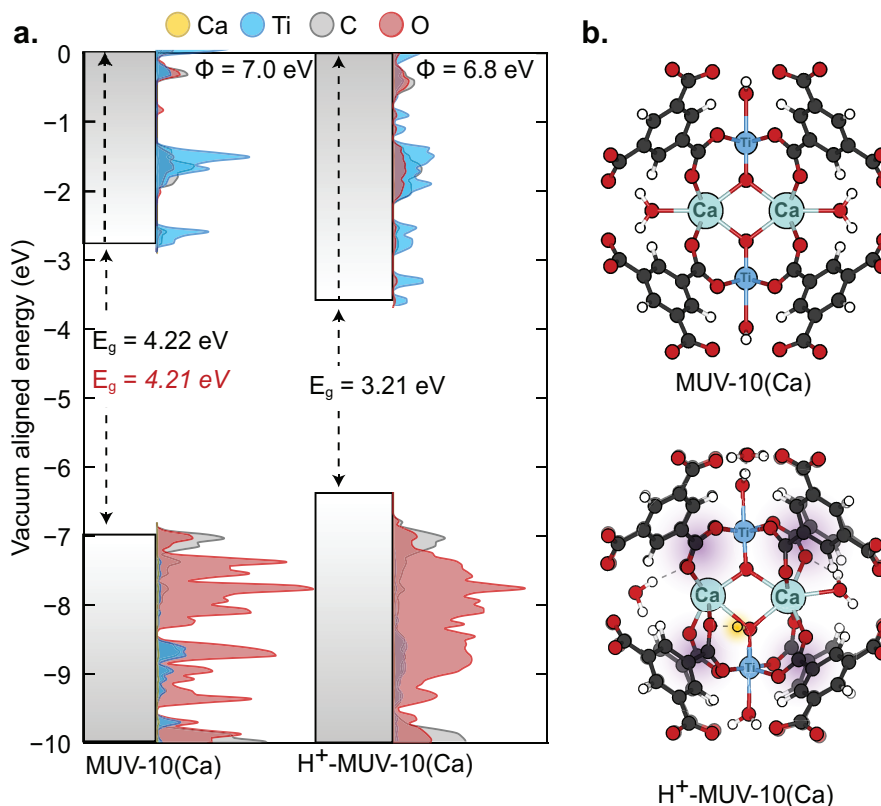


**Figure 10.** a) Computed DOS diagrams and b) optimized structure for hydrated MUV-10(Ca) versus H<sup>+</sup>-MUV-10(Ca).

computed structure of H<sup>+</sup>-MUV-(10) shows considerable disorder around the node, caused by H<sup>+</sup> binding to the oxo bridges (**Fig. 10b**).

**Table 2:** External cation incorporation into MUV-10(Ca) band gap energy comparisons via Tauc plot analysis.

MOF Name	$E_g$ Tauc (eV)
MUV-10 (Ca)	3.83
H <sup>+</sup> -MUV-10 (Ca)	3.22
Li <sup>+</sup> -MUV-10 (Ca)	3.39
K <sup>+</sup> -MUV-10 (Ca)	3.20
Na <sup>+</sup> -MUV-10(Ca)	3.24

*Measurement of light-induced Fermi levels.*

Evidence for tunable band gaps and frontier orbital energies of MUV-10(M) provide a basis for understanding the energetics of Ti-MOF photoredox activity. To complement these

insights, we therefore sought to measure redox potentials of MUV-10(M) during photoredox conditions. Inspired by prior reports of colloidal semiconductor nanocrystals,<sup>61–63</sup> we sought to use a soluble optical redox indicator as a contactless probe of the Fermi-level energy ( $E_F$ ) of MUV-10(M) during photoredox chemistry. This method involves suspending MOFs in solution with a molecule having an electrochemically reversible redox couple that gives rise to distinct sets of optical bands. By allowing the MOF and redox indicator to equilibrate, changes to the UV-vis spectra of the molecule therefore indicate that the MOF has also experienced changes in its redox state, i.e.,  $E_F$ . The absolute absorbance of the optical redox indicator in a given redox state can be related through the appropriate extinction coefficient to its solution concentration. For example, if the absorbance of the reduced state of a molecule decreases, then the new, decreased concentration of the reduced species can be determined. Through the Nernst equation, the ratio of the oxidized and reduced forms of the optical redox indicator can be used to derive a solution  $E_F$ , which is equivalent to the  $E_F$  of the MOF after equilibration. As a proof-of-concept photoredox reaction, we sought to measure the  $E_F$  of MUV-10(M) under photodoping conditions. In brief, the photoredox chemistry would involve the photoexcited MOF oxidizing ethanol, accumulating conduction-band electrons, and exchanging charges with an optical redox indicator (**Fig. 11b**). By monitoring the absorption of the indicator, we would thereby measure the steady-state  $E_F$  *in situ*. In an air-free quartz cuvette, MUV-10(Ca) was suspended in 3 mL of dry acetonitrile with excess ethanol and decamethylferrocenium [ $\text{FeCp}^*_{2^+}$ ] ( $1.5[\text{FeCp}^*_{2^+}]:1\text{Ti}^{4+}$ ) as the optical redox indicator. The mixture was irradiated with a broadband photolysis lamp and the concentration of [ $\text{FeCp}^*_{2^+}$ ] and, hence the [ $\text{FeCp}^*_{2^+}$ ] / [ $\text{FeCp}^*_{2^+}$ ] ratio, was determined from the absorbance at 778 nm, attributable to an LMCT transition of [ $\text{FeCp}^*_{2^+}$ ].<sup>58</sup> **Figure 11a** shows a gradual decrease in the

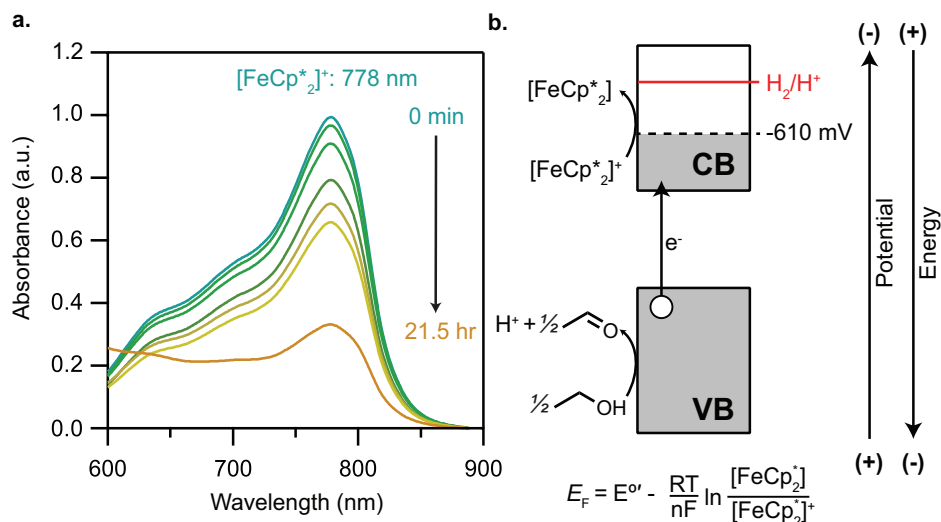


**Figure 11.** Molecular and band-diagram representation of photodoping process in MUV-10(Ca).

absorption bands of  $[\text{FeCp}^*_2]^+$ , indicating photoreduction by MUV-10(Ca). After 21.5 h of irradiation, the system reached steady state, as indicated by no further decrease in absorption bands. Calculating the concentration of  $[\text{FeCp}^*_2]^+$  suggests MUV-10 (M) reduced 33% of the indicator, giving a steady-state redox potential, i.e.,  $E_F$ , of  $-610 \text{ mV}$  vs  $\text{Fc}^+/\text{Fc}$ .<sup>64</sup> Because the photodoping process releases a proton with each electron liberated from ethanol, we expect the  $[\text{H}^+]$  to increase. Based on the assumption that one  $\text{H}^+$  per  $\text{Ti}^{3+}$  is generated in the photoreduction of the indicator, the  $[\text{H}^+]$  can be estimated as  $1.36 \times 10^{-3} \text{ M}$  from the determined concentrations of unreacted  $[\text{FeCp}^*_2]^+$  still in solution at steady state. Hence, these conditions might compare to  $\text{pH} = 2.87$ , albeit in nonaqueous media, where the electrochemical potential for the hydrogen-evolution reaction (HER) sits  $-794 \text{ mV}$  vs  $\text{Fc}^+/\text{Fc}$ . In a similar experiment using instead the cobaltocenium/cobaltocene redox couple ( $-1.33 \text{ V}$  vs  $\text{Fc}^+/\text{Fc}$ ), no photoreduction was observed, which is consistent with the steady-state  $E_F$  of photodoped MUV-10(Ca) being assigned to the milder potential of  $-610 \text{ mV}$  vs  $\text{Fc}^+/\text{Fc}$ .

## Discussion

These results indicate that the frontier orbital energies (band-edge potentials) and band gaps of MUV-10(M) can be tuned by redox-inactive cations. Similar effects have been widely reported for a range of molecular and material systems, including biomimetic models of the oxygen evolving cluster,<sup>49,50</sup> synthetic Fe-oxo complexes,<sup>65,66</sup> polyoxovanadate anions,<sup>51</sup> and semiconductor nanocrystals.<sup>61,62,67–70</sup> In these systems, Lewis acidic ions, e.g.,  $\text{Na}^+$ ,  $\text{Ca}^{2+}$ ,  $\text{Sc}^{3+}$ , modulate redox potentials by hundreds of mV through electrostatic interactions. Whereas harder Lewis acids, such as  $\text{Sc}^{3+}$ , typically induce greater stabilization, the computational results presented here indicate the opposite trend, that MUV-10(Sr) and MUV-10(Ba) exhibited lower Ti-based orbitals than MUV-10(Ca). A key caveat to interpreting this result is that optical absorption energies do not involve nuclear rearrangement in the excited state, while redox potentials are impacted by the nuclear motion associated with ion-pairing.<sup>71</sup> In other words, the stronger influence of harder Lewis acids may be borne out only when they can rearrange to bind more tightly. Instead, we propose that the Ti-based orbitals become stabilized by the larger lattices created by the softer  $\text{Sr}^{2+}$  and  $\text{Ba}^{2+}$  ions. The use of framework- vs external-cations also draws interesting comparisons to the electrostatic impact of redox-inactive cations in degenerately doped semiconductor nanocrystals.<sup>68,72,73</sup> Whereas aliovalent dopants, such as  $\text{Sn}^{4+}$  in  $\text{In}_2\text{O}_3$ , exert greater stabilization on the potentials of delocalized charges compared to surface-bound electrolyte, MOFs lack conventional “bulk” interiors and can be viewed instead entirely as “surface”. Consequently, the introduction of soluble cations had a profound effect on MUV-10(M) band gap energies and electronic structure because every MOF node could be accessed and distorted by the cations. We therefore argue that the electrostatic influence of electrolyte in the pores of MOFs play an important role in determining MOF properties, in general.



Evidence for cation-induced stabilization of Ti-based orbitals helps explain the ability of Ti-MOFs to photodope and trap  $\text{Ti}^{3+}\text{-H}^+$  pairs. Because photodoping of Ti-MOFs involves trapping an electron as  $\text{Ti}^{3+}$  and the liberation of  $\text{H}^+$ , the  $e^-\text{-H}^+$  pair has the potential to recombine as  $\text{H}_2$ , but energetic aspects of the process ensures that it does not. These results support several hypotheses put forward by the Mayer<sup>43</sup> and Martí-Gastaldo<sup>42</sup> labs, and own: First, the calculated geometry of  $\text{H}^+\text{-MUV-10(Ca)}$  indicates localization of  $\text{H}^+$  on bridging oxos and, second, concomitant stabilization of Ti-based conduction-band potentials. Importantly, the *in situ* measurement of  $E_F$  through an optical redox indicator places the steady-state redox potential of photodoped MUV-10(Ca) below the HER electrochemical potential at comparable  $\text{H}^+$  concentrations, providing an energetic justification for the ability of Ti-MOFs to photodope. These experiments involved a rare example of direct reduction of a molecular substrate by a photoexcited MOF node, whereas charges typically transfer from the node to a co-catalyst. Based on these results, we hypothesize that bridging oxo units are generally necessary for Ti-MOFs to stabilize  $\text{H}^+$  against HER. We also expect that photodoped Ti-MOFs will serve as photocatalysts for transferring the  $e^-\text{-H}^+$  pairs to molecular substrates. Previous reports on photocatalysis with Ti-MOFs employed the Ti cluster as a photosensitizer rather than as a site for reactivity, but the availability of OMSs of MUV-10(M), demonstrated here, will allow photoredox chemistry without co-catalysts.

The significant optical changes induced by nitrate salts or by heating may arise from structural disorder surrounding the MUV-10(M) nodes. These results suggest that structural disorder near MOF nodes may play an important role in determining MOF optical absorption properties in general. Introduction of nitrate salts caused the emergence of low-energy bands (**Fig. 9**) and heating gave rise to absorption tails spanning the visible region (**Fig. 6**). Naively, these changes could have been attributed to simple shifts in band-edge potentials rather reordering of

the electronic structures. Computational results suggest that binding of alkali ions to the MUV-10(Ca) node causes a symmetry lowering that introduces mid-gap orbitals. The reversibility of the temperature-induced absorption tails demonstrated in **Figure 5** suggests geometric distortion as well. In a recent study, variable-temperature IR data provided evidence for dynamic metal-linker bonding in MUV-10(Ca) and other common MOFs.<sup>60</sup> At higher temperatures, the metal-carboxylate linkages thermally populate a “loose” configuration that may involve an array of disordered geometries. The energetic degeneracy of the loose geometries could create a high density of mid-gap orbitals that would produce low-energy absorption, akin to Urbach tailing.<sup>74,75</sup> Although typically assumed to be crystalline, defects in MOFs, along with amorphous, liquid, and phase-change MOFs have attracted intense attention recently,<sup>57,76–78</sup> and we propose that disorder near MOF nodes must be considered as well, especially to understand optical behavior.

Finally, these results demonstrate that Tauc analysis is not always appropriate for assigning band gaps to MOFs. In systems with a low DOS, such as molecules and quantum dots, the energy of discrete transitions can be assigned from the peak maxima, often aided by finding the zero-crossing-point of the absorption derivative.<sup>79</sup> Although the majority of MOFs also exhibit low DOS, Tauc analysis is used in nearly all cases. Tauc analysis assumes such a high DOS that the transitions between frontier orbitals cannot be identified, which is typical for amorphous and semiconducting materials.<sup>80,81</sup> Here, we found agreement between experimental and calculated band gap energies for MUV-10(Mn) through Tauc analysis because the charge-transfer bands involving Mn overlapped with those involving the linker and Ti. Tauc analysis was also appropriate for analyzing band gap energies for H<sup>+</sup>-MUV-10(Ca) and other salt-treated variants because disorder at the MOF node introduced a spectrum of overlapping transitions between mid-gap orbitals. For all other MUV-10(M) materials, their wide band gaps and low DOS required

derivative analysis. These results suggest that interpreting the optical behavior of MOFs will require reevaluation of Tauc analysis and the band gap energies it has derived.

## Conclusion

A combined experimental and computational effort indicates that the optical absorption of MUV-10(M) can be tuned by introduction of redox-inactive ions and by structural disorder. On one hand, expanding the MUV-10(M) to include a family of Lewis acid ions ( $\text{Sr}^{2+}$ ,  $\text{Ba}^{2+}$ , and  $\text{Cd}^{2+}$ ) caused stabilization of the frontier orbital energies, compared to the original MUV-10(Ca). On the other hand, the binding of soluble electrolyte cations ( $\text{H}^+$ ,  $\text{Li}^+$ ,  $\text{Na}^+$ ,  $\text{K}^+$ ) to the metal-oxo cluster lowered the symmetry of the material, giving rise to mid-gap orbitals and absorption at longer wavelengths. Previous observations of photodoping ( $\text{Ti}^{3+}$  trapping) of Ti-MOFs can be explained by the stabilization of the Ti-based orbitals by either form of cations. *In situ* optical redox indicators provide direct evidence that the  $\text{Ti}^{3+}\text{-H}^+$  pair remains indefinitely stable because its redox potential sits below that of the hydrogen-evolving reaction. With evidence MUV-10(M) can support open metal sites at the photoactive Ti centers, this family of materials combines key design principles of the oxygen evolving cluster, poising it as a well-defined platform for heterogeneous photoredox chemistry.

## Acknowledgements

We gratefully acknowledge the University of Oregon for startup funds. This work made use of the CAMCOR facility of the Lorry I. Lokey Laboratories at the University of Oregon to perform VT-DRUV-vis experiments. This material is based upon work supported by the National Science Foundation through the Division of Materials Research under grant no. DMR-1956403. We also acknowledge the continued support from the Extreme Science and Engineering Discovery Environment (XSEDE), which is supported by the National Science Foundation [ACI- 1548562]

and the PICS Coeus High Performance Computer, which is supported by the National Science Foundation [1624776].

## References

- (1) Liang, Y.; Zhang, X.; MacMillan, D. W. C. Decarboxylative  $\text{sp}^3$  C-N Coupling via Dual Copper and Photoredox Catalysis. *Nature* **2018**, 559 (7712), 83–88.
- (2) Perry, I. B.; Brewer, T. F.; Sarver, P. J.; Schultz, D. M.; DiRocco, D. A.; MacMillan, D. W. C. Direct Arylation of Strong Aliphatic C–H Bonds. *Nature* **2018**, 560 (7716), 70–75.
- (3) Le, C.; Chen, T. Q.; Liang, T.; Zhang, P.; MacMillan, D. W. C. A Radical Approach to the Copper Oxidative Addition Problem: Trifluoromethylation of Bromoarenes. *Science* **2018**, 360 (6392), 1010–1014.
- (4) Nicewicz, D. A.; MacMillan, D. W. C. Merging Photoredox Catalysis with Organocatalysis: The Direct Asymmetric Alkylation of Aldehydes. *Science* **2008**, 322 (5898), 77–80.
- (5) Linsebigler, A. L.; Lu, G.; Yates, J. T. Photocatalysis on  $\text{TiO}_2$  Surfaces: Principles, Mechanisms, and Selected Results. *Chem. Rev.* **1995**, 95 (3), 735–758.
- (6) Schneider, J.; Matsuoka, M.; Takeuchi, M.; Zhang, J.; Horiuchi, Y.; Anpo, M.; Bahnemann, D. W. Understanding  $\text{TiO}_2$  photocatalysis: Mechanisms and Materials. *Chem. Rev.* **2014**, 114 (19), 9919–9986.
- (7) Fei, H.; Cohen, S. M. A Robust, Catalytic Metal–Organic Framework with Open 2,2'-Bipyridine Sites. *Chem. Commun.* **2014**, 50 (37), 4810–4812.
- (8) Burgess, S. A.; Kassie, A.; Baranowski, S. A.; Fritzsche, K. J.; Schmidt-Rohr, K.; Brown, C. M.; Wade, C. R. Improved Catalytic Activity and Stability of a Palladium Pincer Complex by Incorporation into a Metal–Organic Framework. *J. Am. Chem. Soc.* **2016**, 138 (6), 1780–1783.
- (9) Fei, H.; Cohen, S. M. Metalation of a Thiocatechol-Functionalized Zr(IV)-Based Metal–Organic Framework for Selective C–H Functionalization. *J. Am. Chem. Soc.* **2015**, 137 (6), 2191–2194.
- (10) Dinča, M.; Dailly, A.; Liu, Y.; Brown, C. M.; Neumann, D. A.; Long, J. R. Hydrogen Storage in a Microporous Metal–Organic Framework with Exposed  $\text{Mn}^{2+}$  coordination Sites. *J. Am. Chem. Soc.* **2006**, 128 (51), 16876–16883.
- (11) Feng, X.; Song, Y.; Li, Z.; Kaufmann, M.; Pi, Y.; Chen, J. S.; Xu, Z.; Li, Z.; Wang, C.; Lin, W. Metal–Organic Framework Stabilizes a Low-Coordinate Iridium Complex for Catalytic Methane Borylation. *J. Am. Chem. Soc.* **2019**, 141 (28), 11196–11203.
- (12) Brozek, C. K.; Miller, J. T.; Stoian, S. A.; Dinca, M. NO Disproportionation at a Mononuclear Site-Isolated  $\text{Fe}^{2+}$  Center in  $\text{Fe}^{2+}$ -MOF-5. *J. Am. Chem. Soc.* **2015**, 137 (23), 7495–7501.
- (13) Metzger, E. D.; Brozek, C. K.; Comito, R. J.; Dinca, M. Selective Dimerization of Ethylene to 1-Butene with a Porous Catalyst. *ACS Cent. Sci.* **2016**, 2 (3), 148–153.
- (14) Xiao, D. J.; Bloch, E. D.; Mason, J. A.; Queen, W. L.; Hudson, M. R.; Planas, N.; Borycz, J.; Dzubak, A. L.; Verma, P.; Lee, K.; Bonino, F.; Crocellà, V.; Yano, J.; Bordiga, S.; Truhlar, D. G.; Gagliardi, L.; Brown, C. M.; Long, J. R. Oxidation of Ethane to Ethanol by  $\text{N}_2\text{O}$  in a Metal–Organic Framework with Coordinatively Unsaturated Iron(II) Sites. *Nat. Chem.* **2014**, 6 (7), 590–595.
- (15) Comito, R. J.; Wu, Z.; Zhang, G.; Lawrence, J. A.; Korzyński, M. D.; Kehl, J. A.; Miller,

- J. T.; Dincă, M. Stabilized Vanadium Catalyst for Olefin Polymerization by Site Isolation in a Metal–Organic Framework. *Angew. Chem. Int. Ed.* **2018**, *57* (27), 8135–8139.
- (16) Comito, R. J.; Metzger, E. D.; Wu, Z.; Zhang, G.; Hendon, C. H.; Miller, J. T.; Dincă, M. Selective Dimerization of Propylene with Ni-MFU-4l. *Organometallics* **2017**, *36* (9), 1681–1683.
- (17) Dubey, R. J. C.; Comito, R. J.; Wu, Z.; Zhang, G.; Rieth, A. J.; Hendon, C. H.; Miller, J. T.; Dincă, M. Highly Stereoselective Heterogeneous Diene Polymerization by Co-MFU-4l: A Single-Site Catalyst Prepared by Cation Exchange. *J. Am. Chem. Soc.* **2017**, *139* (36), 12664–12669.
- (18) Metzger, E. D.; Comito, R. J.; Hendon, C. H.; Dincă, M. Mechanism of Single-Site Molecule-like Catalytic Ethylene Dimerization in Ni-MFU-4l. *J. Am. Chem. Soc.* **2017**, *139* (2), 757–762.
- (19) Miner, E. M.; Gul, S.; Ricke, N. D.; Pastor, E.; Yano, J.; Yachandra, V. K.; Van Voorhis, T.; Dincă, M. Mechanistic Evidence for Ligand-Centered Electrocatalytic Oxygen Reduction with the Conductive MOF  $\text{Ni}_3(\text{Hexaiminotriphenylene})_2$ . *ACS Catal.* **2017**, *7* (11), 7726–7731.
- (20) Johnson, B. A.; Bhunia, A.; Ott, S. Electrocatalytic Water Oxidation by a Molecular Catalyst Incorporated into a Metal–Organic Framework Thin Film. *Dalt. Trans.* **2017**, *46* (5), 1382–1388.
- (21) Miner, E. M.; Wang, L.; Dincă, M. Modular  $\text{O}_2$  Electroreduction Activity in Triphenylene-Based Metal–Organic Frameworks. *Chem. Sci.* **2018**, *9* (29), 6286–6291.
- (22) Ding, Q.; Pan, Y.; Luo, Y.; Zhou, M.; Guan, Y.; Li, B.; Trivedi, M.; Kumar, A.; Liu, J. Photocatalytic and Ferric Ion Sensing Properties of a New Three-Dimensional Metal–Organic Framework Based on Cuboctahedral Secondary Building Units. *ACS Omega* **2019**, *4* (6), 10775–10783.
- (23) Pratik, S. M.; Cramer, C. J. Predicted Efficient Visible-Light Driven Water Splitting and Carbon Dioxide Reduction Using Photoredox-Active UiO-NDI Metal Organic Framework. *J. Phys. Chem. C* **2019**, *123* (32), 19778–19785.
- (24) Santiago-Portillo, A.; Remiro-Buenamañana, S.; Navalón, S.; García, H. Subphthalocyanine Encapsulated within MIL-101(Cr)-NH<sub>2</sub> as a Solar Light Photoredox Catalyst for Dehalogenation of  $\alpha$ -Haloacetophenones. *Dalt. Trans.* **2019**, *48* (48), 17735–17740.
- (25) Zhu, Y. Y.; Lan, G.; Fan, Y.; Veroneau, S. S.; Song, Y.; Micheroni, D.; Lin, W. Merging Photoredox and Organometallic Catalysts in a Metal–Organic Framework Significantly Boosts Photocatalytic Activities. *Angew. Chem. Int. Ed.* **2018**, *57* (43), 14090–14094.
- (26) Shi, D.; He, C.; Qi, B.; Chen, C.; Niu, J.; Duan, C. Merging of the Photocatalysis and Copper Catalysis in Metal–Organic Frameworks for Oxidative C–C Bond Formation. *Chem. Sci.* **2015**, *6* (2), 1035–1042.
- (27) Guo, F.; Wei, Y. P.; Wang, S. Q.; Zhang, X. Y.; Wang, F. M.; Sun, W. Y. Pt Nanoparticles Embedded in Flowerlike  $\text{NH}_2$ -UiO-68 for Enhanced Photocatalytic Carbon Dioxide Reduction. *J. Mater. Chem. A* **2019**, *7* (46), 26490–26495.
- (28) Wang, C.; Xie, Z.; Dekrafft, K. E.; Lin, W. Doping Metal–Organic Frameworks for Water Oxidation, Carbon Dioxide Reduction, and Organic Photocatalysis. *J. Am. Chem. Soc.* **2011**, *133* (34), 13445–13454.
- (29) Ji, P.; Manna, K.; Lin, Z.; Urban, A.; Greene, F. X.; Lan, G.; Lin, W. Single-Site Cobalt Catalysts at New  $\text{Zr}_8(\mu_2\text{-O})_8(\text{M}_2\text{-OH})_4$  Metal–Organic Framework Nodes for Highly

- Active Hydrogenation of Alkenes, Imines, Carbonyls, and Heterocycles. *J. Am. Chem. Soc.* **2016**, *138* (37), 12234–12242.
- (30) Ji, P.; Song, Y.; Drake, T.; Veroneau, S. S.; Lin, Z.; Pan, X.; Lin, W. Titanium(III)-Oxo Clusters in a Metal-Organic Framework Support Single-Site Co(II)-Hydride Catalysts for Arene Hydrogenation. *J. Am. Chem. Soc.* **2018**, *140* (1), 433–440.
- (31) Song, Y.; Li, Z.; Zhu, Y.; Feng, X.; Chen, J. S.; Kaufmann, M.; Wang, C.; Lin, W. Titanium Hydroxide Secondary Building Units in Metal–Organic Frameworks Catalyze Hydrogen Evolution under Visible Light. *J. Am. Chem. Soc.* **2019**, *141* (31), 12219–12223.
- (32) Zhang, H.; Lu, Y.; Zhang, Z. M.; Wang, E. B. A Three-Dimensional Metal-Organic Framework Based on Hexanuclear Copper Units with Unsaturated Cu<sup>II</sup> Centers. *Inorg. Chem. Commun.* **2012**, *17*, 9–12.
- (33) Masoomi, M. Y.; Bagheri, M.; Morsali, A.; Junk, P. C. High Photodegradation Efficiency of Phenol by Mixed-Metal-Organic Frameworks. *Inorg. Chem. Front.* **2016**, *3* (7), 944–951.
- (34) Shen, L.; Liang, S.; Wu, W.; Liang, R.; Wu, L. Multifunctional NH<sub>2</sub>-Mediated Zirconium Metal-Organic Framework as an Efficient Visible-Light-Driven Photocatalyst for Selective Oxidation of Alcohols and Reduction of Aqueous Cr(VI). *Dalt. Trans.* **2013**, *42* (37), 13649–13657.
- (35) Wang, D.; Huang, R.; Liu, W.; Sun, D.; Li, Z. Fe-Based MOFs for Photocatalytic CO<sub>2</sub> Reduction: Role of Coordination Unsaturated Sites and Dual Excitation Pathways. *ACS Catal.* **2014**, *4* (12), 4254–4260.
- (36) Guesh, K.; Caiuby, C. A. D.; Mayoral, Á.; Díaz-García, M.; Díaz, I.; Sanchez-Sanchez, M. Sustainable Preparation of MIL-100(Fe) and Its Photocatalytic Behavior in the Degradation of Methyl Orange in Water. *Cryst. Growth Des.* **2017**, *17* (4), 1806–1813.
- (37) Li, G.; Li, F.; Liu, J.; Fan, C. Fe-Based MOFs for Photocatalytic N<sub>2</sub> Reduction: Key Role of Transition Metal Iron in Nitrogen Activation. *J. Solid State Chem.* **2020**, *285* (February), 121245.
- (38) Mason, J. A.; Darago, L. E.; Lukens, W. W.; Long, J. R. Synthesis and O<sub>2</sub> Reactivity of a Titanium(III) Metal-Organic Framework. *Inorg. Chem.* **2015**, *54* (20), 10096–10104.
- (39) Dan-Hardi, M.; Serre, C.; Frot, T.; Rozes, L.; Maurin, G.; Sanchez, C.; Férey, G. A New Photoactive Crystalline Highly Porous Titanium(IV) Dicarboxylate. *J. Am. Chem. Soc.* **2009**, *131* (31), 10857–10859.
- (40) Fu, Y.; Sun, D.; Chen, Y.; Huang, R.; Ding, Z.; Fu, X.; Li, Z. An Amine-Functionalized Titanium Metal-Organic Framework Photocatalyst with Visible-Light-Induced Activity for CO<sub>2</sub> Reduction. *Angew. Chemie - Int. Ed.* **2012**, *51* (14), 3364–3367.
- (41) Hendon, C. H.; Tiana, D.; Fontecave, M.; Sanchez, C.; D'arras, L.; Sassoye, C.; Rozes, L.; Mellot-Draznieks, C.; Walsh, A. Engineering the Optical Response of the Titanium-MIL-125 Metal–Organic Framework through Ligand Functionalization. *J. Am. Chem. Soc.* **2013**, *135* (30), 10942–10945.
- (42) Padial, N. M.; Castells-Gil, J.; Almora-Barrios, N.; Romero-Angel, M.; da Silva, I.; Barawi, M.; García-Sánchez, A.; de la Peña O'Shea, V. A.; Martí-Gastaldo, C. Hydroxamate Titanium–Organic Frameworks and the Effect of Siderophore-Type Linkers over Their Photocatalytic Activity. *J. Am. Chem. Soc.* **2019**, *141* (33), 13124–13133.
- (43) Saouma, C. T.; Tsou, C. C.; Richard, S.; Ameloot, R.; Vermoortele, F.; Smolders, S.; Bueken, B.; Dipasquale, A. G.; Kaminsky, W.; Valdez, C. N.; De Vos, D. E.; Mayer, J. M.

- Sodium-Coupled Electron Transfer Reactivity of Metal-Organic Frameworks Containing Titanium Clusters: The Importance of Cations in Redox Chemistry. *Chem. Sci.* **2019**, *10* (5), 1322–1331.
- (44) Saouma, C. T.; Richard, S.; Smolders, S.; Delley, M. F.; Ameloot, R.; Vermoortele, F.; De Vos, D. E.; Mayer, J. M. Bulk-to-Surface Proton-Coupled Electron Transfer Reactivity of the Metal-Organic Framework MIL-125. *J. Am. Chem. Soc.* **2018**, *140* (47), 16184–16189.
- (45) Cox, N.; Pantazis, D. A.; Neese, F.; Lubitz, W. Biological Water Oxidation. *Acc. Chem. Res.* **2013**, *46* (7), 1588–1596.
- (46) Umena, Y.; Kawakami, K.; Shen, J. R.; Kamiya, N. Crystal Structure of Oxygen-Evolving Photosystem II at a Resolution of 1.9 Å. *Nature* **2011**, *473* (7345), 55–60.
- (47) Mukhopadhyay, S.; Mandal, S. K.; Bhaduri, S.; Armstrong, W. H. Manganese Clusters with Relevance to Photosystem II. *Chem. Rev.* **2004**, *104* (9), 3981–4026.
- (48) Schuth, N.; Zaharieva, I.; Chernev, P.; Berggren, G.; Anderlund, M.; Styring, S.; Dau, H.; Haumann, M. K $\alpha$  X-Ray Emission Spectroscopy on the Photosynthetic Oxygen-Evolving Complex Supports Manganese Oxidation and Water Binding in the S3 State. *Inorg. Chem.* **2018**, *57* (16), 10424–10430.
- (49) Tsui, E. Y.; Tran, R.; Yano, J.; Agapie, T. Redox-Inactive Metals Modulate the Reduction Potential in Heterometallic Manganese–Oxido Clusters. *Nat. Chem.* **2013**, *5* (4), 293–299.
- (50) Tsui, E. Y.; Agapie, T. Reduction Potentials of Heterometallic Manganese-Oxido Cubane Complexes Modulated by Redox-Inactive Metals. *Proc. Natl. Acad. Sci.* **2013**, *110* (25), 10084–10088.
- (51) Greiner, S.; Schwarz, B.; Ringenberg, M.; Dürr, M.; Ivanovic-Burmazovic, I.; Fichtner, M.; Anjass, M.; Streb, C. Redox-Inactive Ions Control the Redox-Activity of Molecular Vanadium Oxides. *Chem. Sci.* **2020**, *11* (17), 4450–4455.
- (52) Kanady, Jacob S, Emily Y, Tsui, Michael W. Day, T. A. A Synthetic Model of the Mn<sub>3</sub>Ca Subsite of the Oxygen-Evolving Complex in Photosystem II. *Science*. **2013**, *733* (2011), 733–737.
- (53) Castells-Gil, J.; Padial, N. M.; Almora-Barrios, N.; Albero, J.; Ruiz-Salvador, A. R.; González-Platas, J.; García, H.; Martí-Gastaldo, C. Chemical Engineering of Photoactivity in Heterometallic Titanium–Organic Frameworks by Metal Doping. *Angew. Chem. Int. Ed.* **2018**, *57* (28), 8453–8457.
- (54) Paul, A.; Borrelli, R.; Bouyanfif, H.; Gottis, S.; Sauvage, F. Tunable Redox Potential, Optical Properties, and Enhanced Stability of Modified Ferrocene-Based Complexes. *ACS Omega* **2019**, *4* (12), 14780–14789.
- (55) Padial, N. M.; Lerma-Berlanga, B.; Almora-Barrios, N.; Castells-Gil, J.; da Silva, I.; de la Mata, M.; Molina, S. I.; Hernández-Saz, J.; Platero-Prats, A. E.; Tatay, S.; Martí-Gastaldo, C. Heterometallic Titanium–Organic Frameworks by Metal-Induced Dynamic Topological Transformations. *J. Am. Chem. Soc.* **2020**, *142* (14), 6638–6648.
- (56) Brozek, C. K.; Dincă, M. Lattice-Imposed Geometry in Metal–Organic Frameworks: Lacunary Zn<sub>4</sub>O Clusters in MOF-5 Serve as Tripodal Chelating Ligands for Ni<sup>2+</sup>. *Chem. Sci.* **2012**, *3* (6), 2110.
- (57) Castells-Gil, J.; M. Padial, N.; Almora-Barrios, N.; Gil-San-Millán, R.; Romero-Ángel, M.; Torres, V.; da Silva, I.; Vieira, B. C. J.; Waerenborgh, J. C.; Jagiello, J.; Navarro, J. A. R.; Tatay, S.; Martí-Gastaldo, C. Heterometallic Titanium–Organic Frameworks as Dual-Metal Catalysts for Synergistic Non-Buffered Hydrolysis of Nerve Agent Simulants.

- Chem* **2020**, *6* (11), 3118–3131.
- (58) Shannon, R. D. Revised Effective Ionic Radii and Systematic Studies of Interatomic Distances in Halides and Chalcogenides. *Acta Crystallogr. Sect. A* **1976**, *32* (5), 751–767.
  - (59) López-Maya, E.; Padial, N. M.; Castells-Gil, J.; R. Ganivet, C.; Rubio-Gaspar, A.; G. Cirujano, F.; Almora-Barrios, N.; Tatay, S.; Navalón, S.; Marti-Gastaldo, C. Selective Implantation of Diamines for Cooperative Catalysis in Isorecticular Heterometallic Titanium-organic Frameworks. *Angew. Chem. Int. Ed.* **2021**, anie.202100176.
  - (60) Andreeva, A. B.; Le, K. N.; Chen, L.; Kellman, M. E.; Hendon, C. H.; Brozek, C. K. Soft Mode Metal-Linker Dynamics in Carboxylate MOFs Evidenced by Variable-Temperature Infrared Spectroscopy. *J. Am. Chem. Soc.* **2020**, *142* (45), 19291–19299.
  - (61) Carroll, G. M.; Schimpf, A. M.; Tsui, E. Y.; Gamelin, D. R. Redox Potentials of Colloidal N-Type ZnO Nanocrystals: Effects of Confinement, Electron Density, and Fermi-Level Pinning by Aldehyde Hydrogenation. *J. Am. Chem. Soc.* **2015**, *137* (34), 11163–11169.
  - (62) Carroll, G. M.; Brozek, C. K.; Hartstein, K. H.; Tsui, E. Y.; Gamelin, D. R. Potentiometric Measurements of Semiconductor Nanocrystal Redox Potentials. *J. Am. Chem. Soc.* **2016**, *138* (13), 4310–4313.
  - (63) Carroll, G. M.; Tsui, E. Y.; Brozek, C. K.; Gamelin, D. R. Spectroelectrochemical Measurement of Surface Electrostatic Contributions to Colloidal CdSe Nanocrystal Redox Potentials. *Chem. Mater.* **2016**, *28* (21), 7912–7918.
  - (64) Connelly, N. G.; Geiger, W. E. Chemical Redox Agents for Organometallic Chemistry. *Chem. Rev.* **1996**, *96* (2), 877–910.
  - (65) Morimoto, Y.; Kotani, H.; Park, J.; Lee, Y. M.; Nam, W.; Fukuzumi, S. Metal Ion-Coupled Electron Transfer of a Nonheme Oxoiron(IV) Complex: Remarkable Enhancement of Electron-Transfer Rates by  $\text{Sc}^{3+}$ . *J. Am. Chem. Soc.* **2011**, *133* (3), 403–405.
  - (66) Fukuzumi, S.; Morimoto, Y.; Kotani, H.; Naumov, P.; Lee, Y.-M.; Nam, W. Crystal Structure of a Metal Ion-Bound Oxoiron(IV) Complex and Implications for Biological Electron Transfer. *Nat. Chem.* **2010**, *2* (9), 756–759.
  - (67) Brozek, C. K.; Hartstein, K. H.; Gamelin, D. R. Potentiometric Titrations for Measuring the Capacitance of Colloidal Photodoped ZnO Nanocrystals. *J. Am. Chem. Soc.* **2016**, *138* (33), 10605–10610.
  - (68) Brozek, C. K.; Zhou, D.; Liu, H.; Li, X.; Kittilstved, K. R.; Gamelin, D. R. Soluble Supercapacitors: Large and Reversible Charge Storage in Colloidal Iron-Doped ZnO Nanocrystals. *Nano Lett.* **2018**, *18* (5), 3297–3302.
  - (69) Schimpf, A. M.; Ochsenbein, S. T.; Buonsanti, R.; Milliron, D. J.; Gamelin, D. R. Comparison of Extra Electrons in Colloidal N-Type  $\text{Al}^{3+}$ -Doped and Photochemically Reduced ZnO Nanocrystals. *Chem. Commun.* **2012**, *48* (75), 9352.
  - (70) Schimpf, A. M.; Knowles, K. E.; Carroll, G. M.; Gamelin, D. R. Electronic Doping and Redox-Potential Tuning in Colloidal Semiconductor Nanocrystals. *Acc. Chem. Res.* **2015**, *48* (7), 1929–1937.
  - (71) Boettcher, S. W.; Oener, S. Z.; Lonergan, M. C.; Surendranath, Y.; Ardo, S.; Brozek, C.; Kempler, P. A. Potentially Confusing: Potentials in Electrochemistry. *ACS Energy Lett.* **2021**, *6* (1), 261–266.
  - (72) Liu, H.; Brozek, C. K.; Sun, S.; Lingerfelt, D. B.; Gamelin, D. R.; Li, X. A Hybrid Quantum-Classical Model of Electrostatics in Multiply Charged Quantum Dots. *J. Phys. Chem. C* **2017**, *121* (46), 26086–26095.



- (73) Hartstein, K. H.; Brozek, C. K.; Hinterding, S. O. M.; Gamelin, D. R. Copper-Coupled Electron Transfer in Colloidal Plasmonic Copper-Sulfide Nanocrystals Probed by in Situ Spectroelectrochemistry. *J. Am. Chem. Soc.* **2018**, *140* (9), 3434–3442.
- (74) John, S.; Soukoulis, C.; Cohen, M. H.; Economou, E. N. Theory of Electron Band Tails and the Urbach Optical-Absorption Edge. *Phys. Rev. Lett.* **1986**, *57* (14), 1777–1780.
- (75) Ikhmayies, S. J.; Ahmad-Bitar, R. N. A Study of the Optical Bandgap Energy and Urbach Tail of Spray-Deposited CdS:In Thin Films. *J. Mater. Res. Technol.* **2013**, *2* (3), 221–227.
- (76) Abánades Lázaro, I.; Almora-Barrios, N.; Tatay, S.; Martí-Gastaldo, C. Effect of Modulator Connectivity in Promoting Defectivity in Titanium-Organic Frameworks. *Chem. Sci.* **2021**, *68* (20), 42–61.
- (77) Lee, S.; Bürgi, H.-B.; Alshimri, S. A.; Yaghi, O. M. Impact of Disordered Guest–Framework Interactions on the Crystallography of Metal–Organic Frameworks. *J. Am. Chem. Soc.* **2018**, *140* (28), 8958–8964.
- (78) Cheetham, A. K.; Bennett, T. D.; Coudert, F.-X.; Goodwin, A. L. Defects and Disorder in Metal Organic Frameworks. *Dalt. Trans.* **2016**, *45* (10), 4113–4126.
- (79) Zanatta, A. R. Revisiting the Optical Bandgap of Semiconductors and the Proposal of a Unified Methodology to Its Determination. *Sci. Rep.* **2019**, *9* (1), 11225.
- (80) Dolgonos, A.; Mason, T. O.; Poeppelmeier, K. R. Direct Optical Band Gap Measurement in Polycrystalline Semiconductors: A Critical Look at the Tauc Method. *J. Solid State Chem.* **2016**, *240*, 43–48.
- (81) Tauc, J. Optical Properties and Electronic Structure of Amorphous Ge and Si. *Mater. Res. Bull.* **1968**, *3* (1), 37–46.